PLOS BIOLOGY

SHORT REPORTS

Morphology of mitochondria in spatially restricted axons revealed by cryo-electron tomography

Tara D. Fischer[1,2¤a], **Pramod K. Dash**[1,3], **Jun Liu**[4¤b], **M. Neal Waxham**[1]*

1 Department of Neurobiology and Anatomy, McGovern Medical School, University of Texas Health Science Center at Houston, Houston, Texas, United States of America, **2** The University of Texas MD Anderson Cancer Center UTHealth Graduate School of Biomedical Sciences, The University of Texas Health Science Center at Houston, Houston, Texas, United States America, **3** Vivian L. Smith Department of Neurosurgery, McGovern Medical School, University of Texas Health Science Center at Houston, Houston, Texas, United States of America, **4** Department of Pathology and Laboratory Medicine, McGovern Medical School, University of Texas Health Science Center at Houston, Houston, Texas, United States of America

¤a Current address: Biochemistry Section, Surgical Neurology Branch, National Institute of Neurological Disorders and Stroke, National Institutes of Health, Bethesda, Maryland, United States of America
¤b Current address: Department of Microbial Pathogenesis & Microbial Sciences Institute, Yale School of Medicine, New Haven, Connecticut, United States of America
* m.n.waxham@uth.tmc.edu

Citation: Fischer TD, Dash PK, Liu J, Waxham MN (2018) Morphology of mitochondria in spatially restricted axons revealed by cryo-electron tomography. PLoS Biol 16(9): e2006169. https://doi.org/10.1371/journal.pbio.2006169

Academic Editor: Matthew Dalva, Thomas Jefferson University, United States of America

Received: March 27, 2018

Accepted: September 5, 2018

Published: September 17, 2018

Data Availability Statement: All relevant data are within the paper and its Supporting Information files.

Funding: National Institute of Health/National Institute of Neurological Disease and Stroke (grant number R01NS101686). PKD and MNW. The funder had no role in study design, data collection and analysis, decision to publish, or preparation of the manuscript. National Institute of Health/National Institute of Neurological Disease and Stroke (grant number R01NS087149). PKD. The funder had no role in study design, data collection

Abstract

Neurons project axons to local and distal sites and can display heterogeneous morphologies with limited physical dimensions that may influence the structure of large organelles such as mitochondria. Using cryo-electron tomography (cryo-ET), we characterized native environments within axons and presynaptic varicosities to examine whether spatial restrictions within these compartments influence the morphology of mitochondria. Segmented tomographic reconstructions revealed distinctive morphological characteristics of mitochondria residing at the narrowed boundary between presynaptic varicosities and axons with limited physical dimensions (approximately 80 nm), compared to mitochondria in nonspatially restricted environments. Furthermore, segmentation of the tomograms revealed discrete organizations between the inner and outer membranes, suggesting possible independent remodeling of each membrane in mitochondria at spatially restricted axonal/varicosity boundaries. Thus, cryo-ET of mitochondria within axonal subcompartments reveals that spatial restrictions do not obstruct mitochondria from residing within them, but limited available space can influence their gross morphology and the organization of the inner and outer membranes. These findings offer new perspectives on the influence of physical and spatial characteristics of cellular environments on mitochondrial morphology and highlight the potential for remarkable structural plasticity of mitochondria to adapt to spatial restrictions within axons.

and analysis, decision to publish, or preparation of the manuscript. National Institute of Health/ National Institute of Neurological Disease and Stroke (grant number F31NS098790). TDF, Ruth L. Kirchstein National Research Service Award Predoctoral Fellowship. The funder had no role in study design, data collection and analysis, decision to publish, or preparation of the manuscript. National Institute of Health (grant number S10OD016279). MNW, Structural Biology Imaging Center at UTHSC—Houston. The funder had no role in study design, data collection and analysis, decision to publish, or preparation of the manuscript.

Competing interests: The authors have declared that no competing interests exist.

Abbreviations: CaMKIIα, calcium/calmodulin-dependent protein kinase II alpha; cryo-ET, cryo-electron tomography; EM, electron microscopy; ER, endoplasmic reticulum; IBM, inner boundary membrane; IMM, inner mitochondrial membrane; MICOS, mitochondrial contact site and cristae organizing system; Miro, Mitochondrial Rho GTPase; MVB, multivesicular body; OMM, outer mitochondrial membrane; Opa1, optic atrophy 1.

Author summary

Neurons are complex cells that communicate with each other via axons that can extend over distances of a meter or longer. Axons place enormous demands on neuronal energy production, and to maintain connections with local and distal targets, neurons have efficient systems that transport mitochondria to areas of high energy consumption. However, axons show variable dimensions, sometimes thinning to a diameter significantly smaller than the standard diameter of mitochondria, raising the question of how mitochondrial structures can adapt to the local spatial environment. In the present study, we employed electron tomography to investigate the physical and structural relationships between thin axons and the mitochondria that reside within them. We discovered that mitochondria exhibit a remarkable constriction of outer and inner membrane structure in regions of restricted physical dimensions of the axonal space. These findings highlight the remarkable structural plasticity of mitochondria and the potential influence of available space within cells on the structure of mitochondria. Given that maintaining a population of properly localized mitochondria is necessary to support synaptic function, the findings also suggest an adaptive role for mitochondrial structure in facilitating efficient axonal transport.

Introduction

Neurons are architecturally complex cells that can extend axonal projections with elaborate arborization for several hundreds of millimeters (and in some cases, meters) to form synaptic connections with local and distal targets [1–3]. Depending on the target, presynaptic compartments can either be found at the end of axons (terminal boutons) or tracking along axons as intermediate swellings (en passant boutons or varicosities), such as in the unmyelinated CA3->CA1 axons of the hippocampus [3–7]. The bead-like presynaptic varicosities are morphologically heterogeneous, displaying diameters that can range from 1 to 2 μm connected by thin axon segments that can have diameters less than 100 nm [4,5,8,9].

Tracking through the axons is a well-developed system of microtubules that mediate motor-driven anterograde and retrograde transport of signaling cargoes, protein complexes, and organelles critical for function and homeostasis at distant synapses [10,11]. Transport of these intracellular components creates a spatially and temporally dynamic environment within the axon that can contain a variety of organelles and cargoes of different shapes, sizes, and number [12,13]. As axon segments interconnecting varicosities can be remarkably thin and occupied by various structures, whether physical adaptations to available space are required for the motility of large organelles such as mitochondria, with diameters ranging between 100 and 500 nm, poses an interesting question [14,15]. Mitochondria within axons and synaptic compartments are particularly critical for development, function, and plasticity. During transport, mitochondria are known to make frequent stops, or saltatory movements, at presynaptic compartments to provide local ATP synthesis and calcium regulation required for proper neurotransmission [16–20]. Given the morphological complexity of axons, restricted physical dimensions and available space could potentially influence the subcellular localization, distribution, and transport of mitochondria required to meet local energy needs and for supporting synaptic transmission. Although mitochondria are morphologically dynamic organelles that can exist in a variety of shapes and sizes, how mitochondria adapt to the physical constraints presented in axons has not been previously examined.

Advances in microscopy and imaging techniques have played a pivotal role in revealing the three-dimensional (3D) architecture of neurons and their intracellular environments at resolutions reaching the nanometer scale [21,22]. In the current study, we employed cryo-electron tomography (cryo-ET) to visualize 3D spatial relationships and organellar structure within cultured hippocampal axons and varicosities. The unique native state preservation afforded by cryopreservation and the resolution of cryo-ET revealed that axon morphology and physically restrictive intracellular dimensions present a previously unrecognized influence on the morphology and ultrastructure of mitochondria residing at the boundary between large varicosities and small axonal subcompartments.

Results

Preparation of primary hippocampal neurons for cryo-ET

Primary neuronal cultures from E18 rat hippocampi were grown on holey carbon grids prior to cryo-preservation. At 10 d post plating, primary hippocampal neurons have extended dendritic and axonal processes and have established presynaptic varicosities and initial excitatory synaptic connections [23]. Fig 1A and 1B show representative bright-field images of neurons cultured on a Quantifoil grid where widespread elaboration of processes is evident. Fig 1C and 1D demonstrate images of companion grids that were fixed and immunolabeled with antibodies to calcium/calmodulin-dependent protein kinase II alpha (CaMKIIα) and synapsin 1 to visualize the excitatory neuron population and presynaptic varicosities, respectively. CaMKIIα antibodies largely label soma and processes, whereas the synapsin 1 antibody shows distinct puncta representing enrichment of synaptic vesicles at presynaptic varicosities.

For cryo-ET, fiducial gold markers were applied to prepared grids to aid in image alignment during data acquisition and image processing and then cryopreserved by plunge freezing in liquid ethane. Cryopreservation conserves the near-native state of the preparation, permitting an assessment of spatial relationships between organelles present in different neuronal compartments free of fixation- or stain-induced artifacts. Low-magnification images were first collected (Fig 1E) and montaged to provide maps for targeting areas of interest for data collection. A higher-magnification image reveals the distribution of presynaptic varicosities and axonal processes (Fig 1F). Varicosities and axons can be seen both residing on the carbon and overlying the grid holes. To provide maximum contrast, tomographic data collection was targeted to cryopreserved structures within the grid holes. In these preparations, the increased thickness of the soma and proximal dendrites prevented sufficient electron beam penetration for imaging of these structures. In contrast, the sample thickness surrounding the axonal processes and varicosities was ideal, permitting a detailed assessment of the spatial relationships of cytoskeletal structures and organelles within these subcompartments.

Organelle populations of presynaptic varicosities in primary hippocampal neurons are heterogeneous

Areas were randomly chosen, and tilt series were collected from varicosities and axon segments overlying grid holes to visualize cytoskeletal and organellar structures. Fig 2A shows a slice through a representative tomographic reconstruction with various resident organelles and structures visible, including 2 mitochondria, a multivesicular body (MVB), microtubules, endoplasmic reticulum (ER), and a collection of vesicles. Supplementary S1 Fig shows 2D images of identified organelles and other structures observed within the population of varicosities analyzed. To determine the 3D relationship between the different structures, segmentation was accomplished of the tomographic reconstruction of both the presynaptic varicosity and

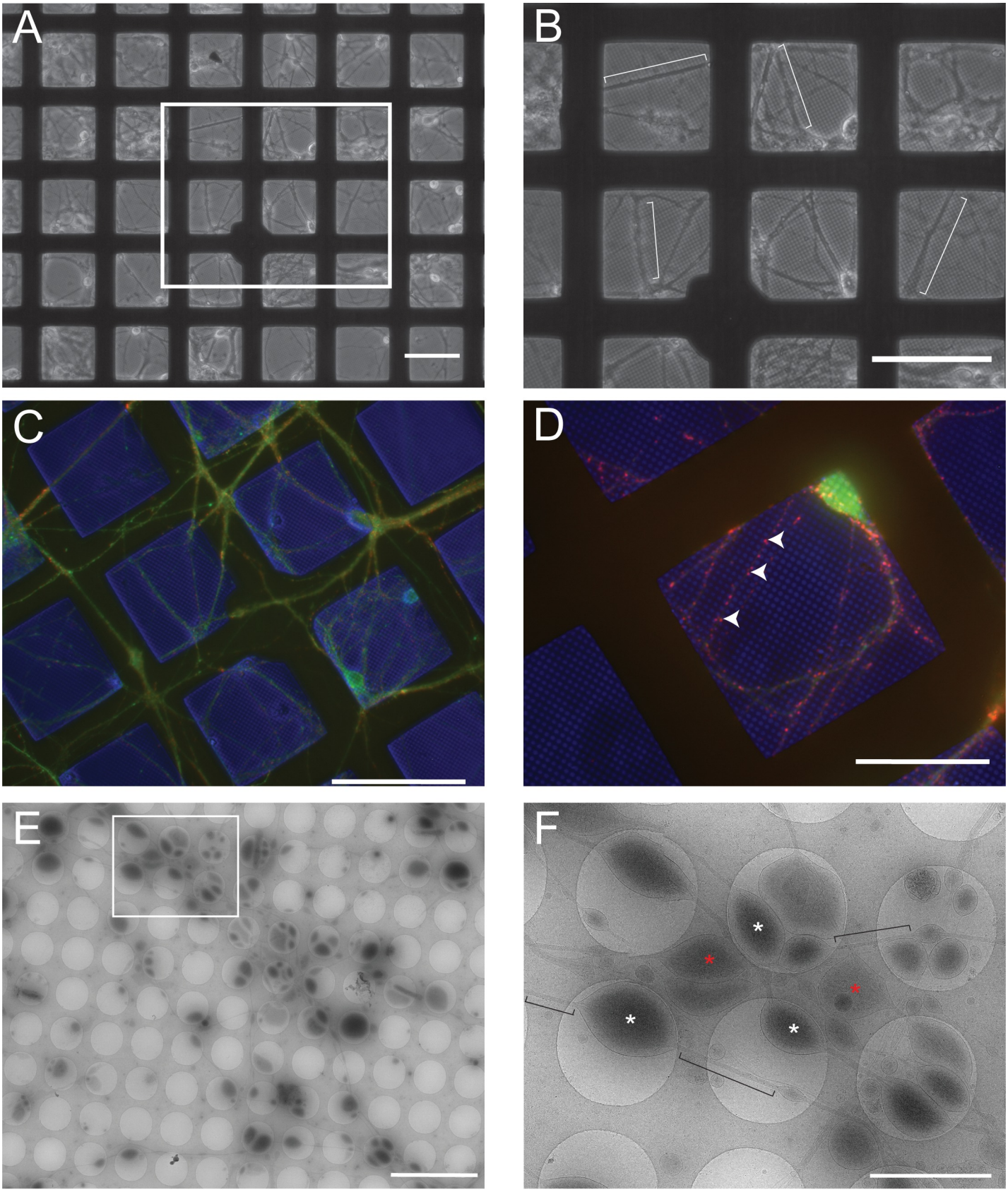
A
B
C
D
E
F

Fig 1. Growth and characterization of primary hippocampal neurons on EM grids. Hippocampal neurons were isolated from E18 rats and plated on poly-D-lysine-coated Quantifoil 2/1 gold grids. (A) Low-magnification bright-field image showing the typical distribution of neuronal soma and processes after 10 d in culture. (B) Higher-magnification image of the area from the white box in panel (A) with neuronal processes highlighted by white brackets. (C) Wide-field fluorescence image showing immunolabeling of the neuron-specific protein CaMKIIα in green and the presynaptic vesicle–associated protein synapsin 1 in red. The blue color is from a bright-field overlay of the same area that also highlights the bars of the EM grid. (D) Higher-magnification image in a different area of the same immunolabeled grid highlighting the punctate staining of synapsin I (red; arrowheads) along processes typical of en passant varicosities in hippocampal axons. Blue is again from where the grid bars and holes in the Quantifoil grid are apparent. Scale bars in panels A–C = 100 μm and in panel D = 50 μm. (E) Low-magnification montage of 1 area in a cryopreserved grid of hippocampal neurons 10 d post plating, showing the typical distribution of axons and synaptic varicosities. Scale bar = 10 μm. (F) Higher-magnification representation from (E; white box) showing the axon and varicosity distribution overlying carbon (slightly darker areas) and grid holes. Examples of varicosities lying within grid holes are marked with white asterisks, whereas examples lying on the carbon are marked with red asterisks. Axon segments interconnecting the varicosities are highlighted with black brackets. Scale bar = 2 μm. CaMKIIα, calcium/calmodulin-dependent protein kinase II alpha; EM, electron microscopy.

https://doi.org/10.1371/journal.pbio.2006169.g001

the adjoining axon (Fig 2B; S1 Movie). The reconstruction demonstrates microtubules (light blue) forming a continuous set of tracks traveling from one end of the varicosity to the other. Microtubules are well organized and relatively straight in axons; however, they exhibit greater curvature in the varicosity while again gathering together and straightening when passing through the adjoining axon segment. The ER (yellow) also forms a reticulated and continuous structure spanning the entire length of the varicosity, consistent with other reports on the ubiquitous presence of ER in axons and synaptic terminals [21]. Mitochondria, MVB, and other sac-like compartments exhibit more random distributions within the varicosity, whereas vesicles appeared to be somewhat clustered. To determine if the presence of each of these identifiable organelles was consistent across varicosities, we analyzed their distribution and

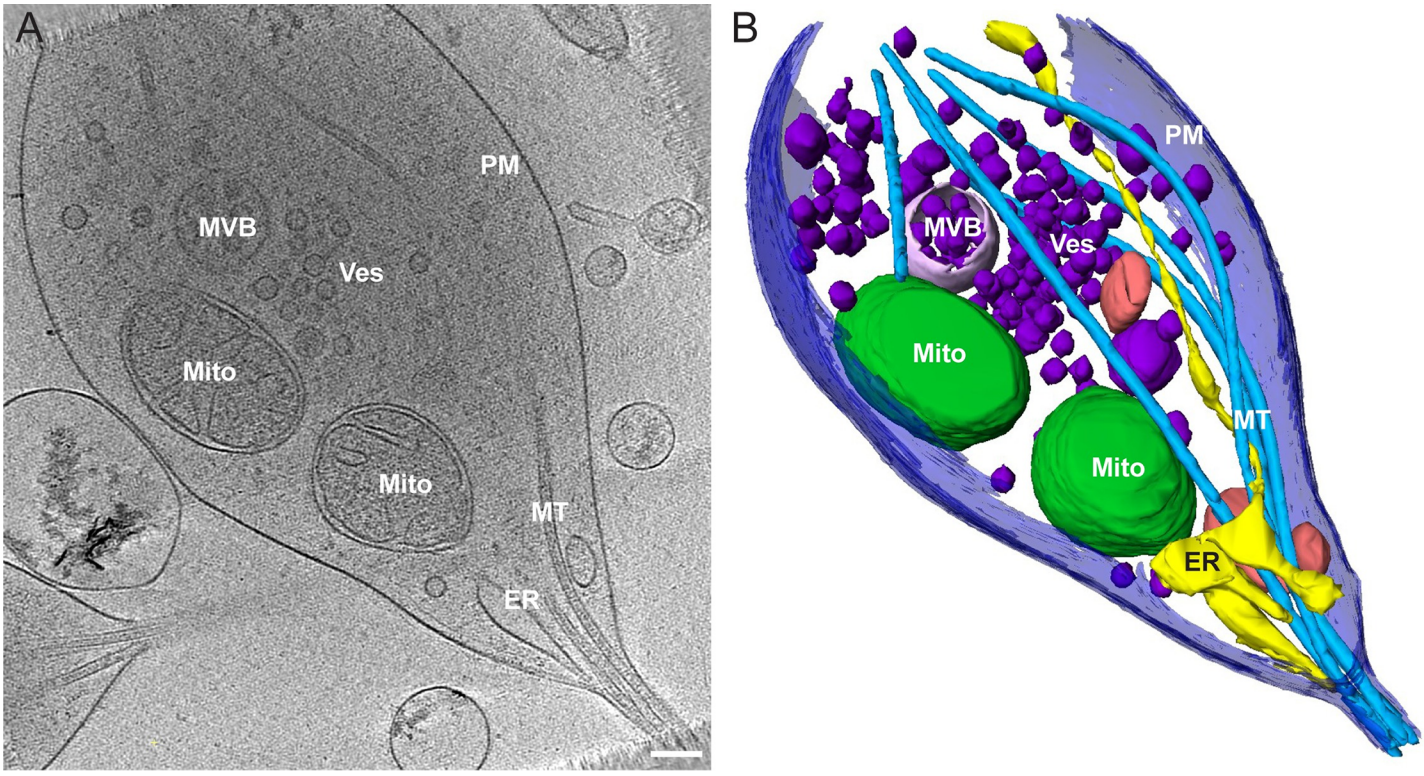

Fig 2. Tomographic reconstruction of a typical presynaptic varicosity and adjoining axon segment. (A) A 2D slice from the tomographic reconstruction showing the distribution of organelles in the varicosity (Mito = mitochondrion). Scale bar = 200 nm. (B) Segmented representation of the entire 3D tomogram volume shown in (A) revealing the relative size and spatial distribution of the organelle environment in the varicosity and axon segment. PM (dark blue), MT (light blue), mitochondrial outer membrane ("Mito," dark green), ER (yellow), Ves (dark purple), MVB (light purple), unidentified membrane-bound compartment (pink). Scale bar = 200 nm. ER, endoplasmic reticulum; MVB, multivesicular body; MT, microtubules; PM, plasma membrane; Ves, vesicle.

https://doi.org/10.1371/journal.pbio.2006169.g002

characteristics in an additional 77 tomographic reconstructions. ER and microtubules were present in 100% of presynaptic varicosities, vesicles were present in 97%, mitochondria in 82%, sac-like compartments in 38%, MVBs in 21%, lamellar bodies in 9%, and autophagosomes in 4% (Table 1).

Variations in distinct subfeatures of the observed organelle populations also emerged in 3D at high resolution. Specifically, the ubiquitous ER was observed in close apposition to almost every other organelle within the varicosities, consistent with ER–membrane contact sites described by others [21]. The vesicular population was heterogeneous in number, ranging from 1 to >100 vesicles per varicosity. Of the varicosities, 75% contained <50 vesicles, 10% had 50–100, and 6% contained more than 100 (Table 1). The mitochondrial cristae structure within the 3D tomographic data sets was variable but could be broadly segregated into 2 distinct populations based on ultrastructural features (S2 Fig). A population of mitochondria displayed the canonical thin, tubular cristae morphology (S2A Fig), whereas a second population displayed thick, unstructured cristae (S2B Fig).

In contrast to the heterogeneous appearance and distribution of organelles in presynaptic varicosities, the adjoining axonal segments were more consistent in composition. The most obvious components were microtubules that were seen as continuous elements, gathered at the sites of axonal narrowing at both ends of the varicosity. Microtubules did not display variability in diameter (approximately 20 nm); however, they did vary in number among different processes and occupied a significant portion of the available volume within the axon. As

Table 1. Organelle population representations.

	Presence within population (%) $n = 77$
Mitochondria	81.8
Number/varicosity	
0	18.1
1	66.2
>1	15.5
Gross morphology	
Round	26.3
Slightly tubular	30.2
Tubular	43.4
Internal morphology	
Thin, tubulated	23.6
Thick, unstructured	76.3
Endoplasmic reticulum	100
Contact with mitochondria	38.4
Near mitochondria	89.7
Vesicles	97.4
Number/cell	
1–25	2.5
25–50	64.9
50–100	10.3
>100	6.4
Multivesicular bodies	20.7
Lamellar bodies	9.0
Unidentified membrane-bound compartments	37.6
Autophagosome	38.9

https://doi.org/10.1371/journal.pbio.2006169.t001

noted, microtubules are the essential tracks required for motor-driven organelle transport and are critical for maintaining synaptic homeostasis and neuronal signaling. The corresponding microtubule occupation of axonal space leaves the qualitative impression that the available volume in axons to accommodate large organelles, such as mitochondria, might be an underappreciated constraint affecting transport. The magnitude of this spatial constraint can be visually appreciated in S2 Movie.

Mitochondria display distinct morphological features at spatially restricted axon/varicosity boundaries

Previous electron microscopy (EM) studies have reported an average axonal diameter between 0.08 and 0.4 μm for unmyelinated cortical axons and an average varicosity diameter of approximately 1–2 μm [1,5,7,8]. Varicosities and axons in our cryopreserved hippocampal preparations exhibited slightly smaller Feret diameters, with an average of 649 and 81 nm for varicosities and axons, respectively (Table 2). Additionally, the average Feret diameter of mitochondria observed in hippocampal varicosities was approximately 250 nm. These dimensions (summarized in Table 2) further reinforce the idea that significant spatial constraints exist that may influence mitochondrial structure in axons.

For more in-depth investigation of this issue, high-magnification tomographic data were collected targeting mitochondria residing at the boundary where the varicosity narrows into the small axonal segment. Whereas such precise mitochondrial positioning was rare in the cryo-preserved neuronal population, the static events that were captured revealed distinct mitochondrial morphologies at the boundaries between varicosities and axons. S3 and S4 Movie demonstrate a mitochondrion partially residing in both a neuronal varicosity and the adjoining axon segment among the other organelles occupying space in these compartments. The portion of the mitochondrion residing in the varicosity is 305 nm in Feret diameter, whereas the portion of the mitochondrion residing in the axonal segment is narrowed to only 70 nm in diameter at its tip. Thus, the mitochondrion displays a major morphological change with an approximately 77% reduction in diameter within the axon. Fig 3A shows a snapshot of the segmented mitochondrion as well as additional examples of mitochondria captured at the varicosity/axonal boundary (Fig 3B and 3C). Fig 3C shows a reconstruction that revealed 2 mitochondria residing in the varicosity and adjoining axon segment, with a portion of a third residing mainly in the axon. S3–S10 Movies demonstrate several tomographic reconstructions of mitochondria displaying similar morphologies at the varicosity/axon boundary. Fig 4 and S9 Movie show a particularly revealing example in which a mitochondrion was captured bridging a short (100 nm in length) axon segment between 2 varicosities. The short, narrow space produced a barbell-shaped mitochondrion with a diameter between 200 and 300 nm in both varicosities, whereas the portion spanning the axon segment was only 19 nm in diameter. To

Table 2. Two-dimensional morphological measures.

	n	Average	Range
Varicosity			
Diameter	200	649 ± 241 nm	257 nm–1.65 μm
Axon			
Diameter	195	81 ± 27 nm	33–204 nm
Mitochondria			
Length	67	647 ± 305 nm	255 nm–1.68 μm
Diameter	71	291 ± 87 nm	160–547 nm

https://doi.org/10.1371/journal.pbio.2006169.t002

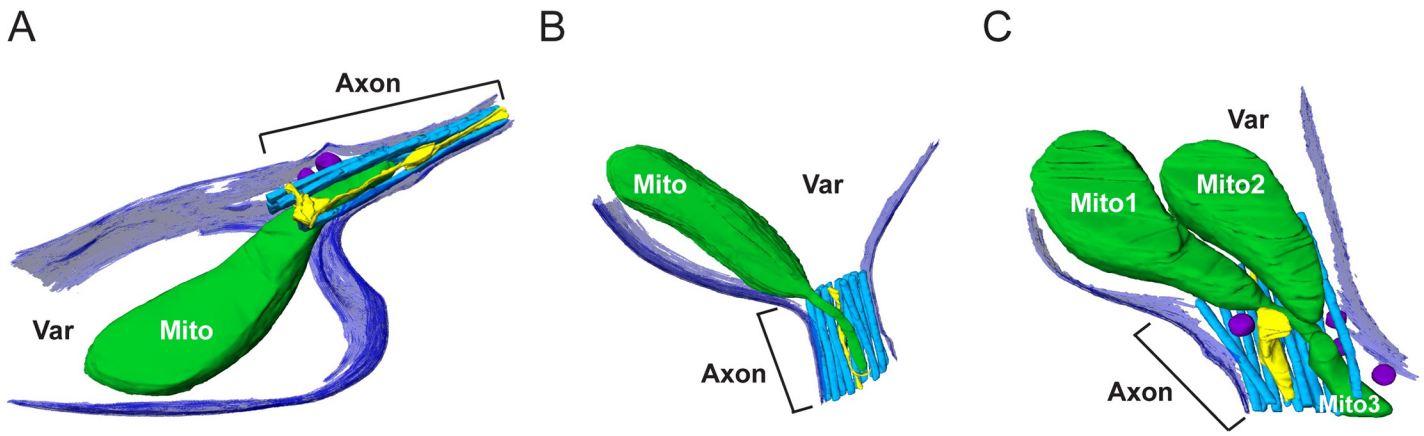

Fig 3. Mitochondria display atypical morphological features in physically restrictive axons. (A–C) Three different 3D segmented reconstructions showing representative examples of mitochondria ("Mito1," "Mito2," and "Mito3") residing partially in the varicosity ("Var") and adjoining axon segments, demonstrating different morphological states at the transition from the varicosity into the restricted space of the axon segment. Additional organelles occupying the axon space are also segmented. For ease of visualization, not all of the organelles and structures in the varicosity are shown. The plasma membrane (dark blue), microtubules (light blue), mitochondrial outer membrane (dark green), endoplasmic reticulum (yellow), and vesicles (dark purple) are highlighted.

https://doi.org/10.1371/journal.pbio.2006169.g003

illustrate the ultrastructural features of the mitochondrion spanning the 2 varicosities, the inner mitochondrial membrane (IMM) and cristae were segmented in addition to the outer mitochondrial membrane (OMM; Fig 4C). The resolution of this tomographic reconstruction was not sufficient to determine whether the IMM was continuous through the short axon segment; however, S10 Movie demonstrates an additional example of a mitochondrion spanning a short axon segment between 2 varicosities, in which the IMM appears continuous in the constricted section of the axon. Analysis of 8 mitochondria exhibiting these drastic morphological features revealed an average of 84% (n = 8, SD = 6%) reduction in the Feret diameter of the mitochondrial area in the varicosity relative to the adjoining axon segment. These captured events highlight the potential adaptability of mitochondrial morphology to accommodate the available space within an axon. Note that in all of the segmented tomographic reconstructions in Figs 3 and 4, the presence of microtubules and additional organelles, such as the ER, further restricts the available volume to mitochondria within axons.

Mitochondrial membranes display unique organizations within spatially restrictive axons

Mitochondrial ultrastructure is thought to be dynamic with remodeling of the inner membrane and formation of specified subcompartments, termed cristae [24–26]. Given the atypical gross morphologies of mitochondria we observed between varicosities and the adjoining axonal segments, we questioned if the IMM also displays distinct structural features in axons with limited physical dimensions. To address this issue, the OMM and IMM captured at the boundary between varicosities and adjoining axons were segmented, separating the outer membrane and 2 regional components of the IMM—the inner boundary membrane (IBM) and the cristae. A conservative approach was taken during manual segmentation of cristae (i.e., only clearly discernible cristae membranes were included). Segmentation of each of these mitochondrial components revealed discrete morphologies between the inner and outer membranes. Most notably, 2 distinctions were observed between the outer membrane and the adjacent IBM at the narrowed mitochondrial tip in the adjoining axon segment. First, in some instances, the IBM was observed to maintain apposition to the outer membrane at the narrowed mitochondrial tip entering the axon (Fig 5A). Both the inner (orange) and outer

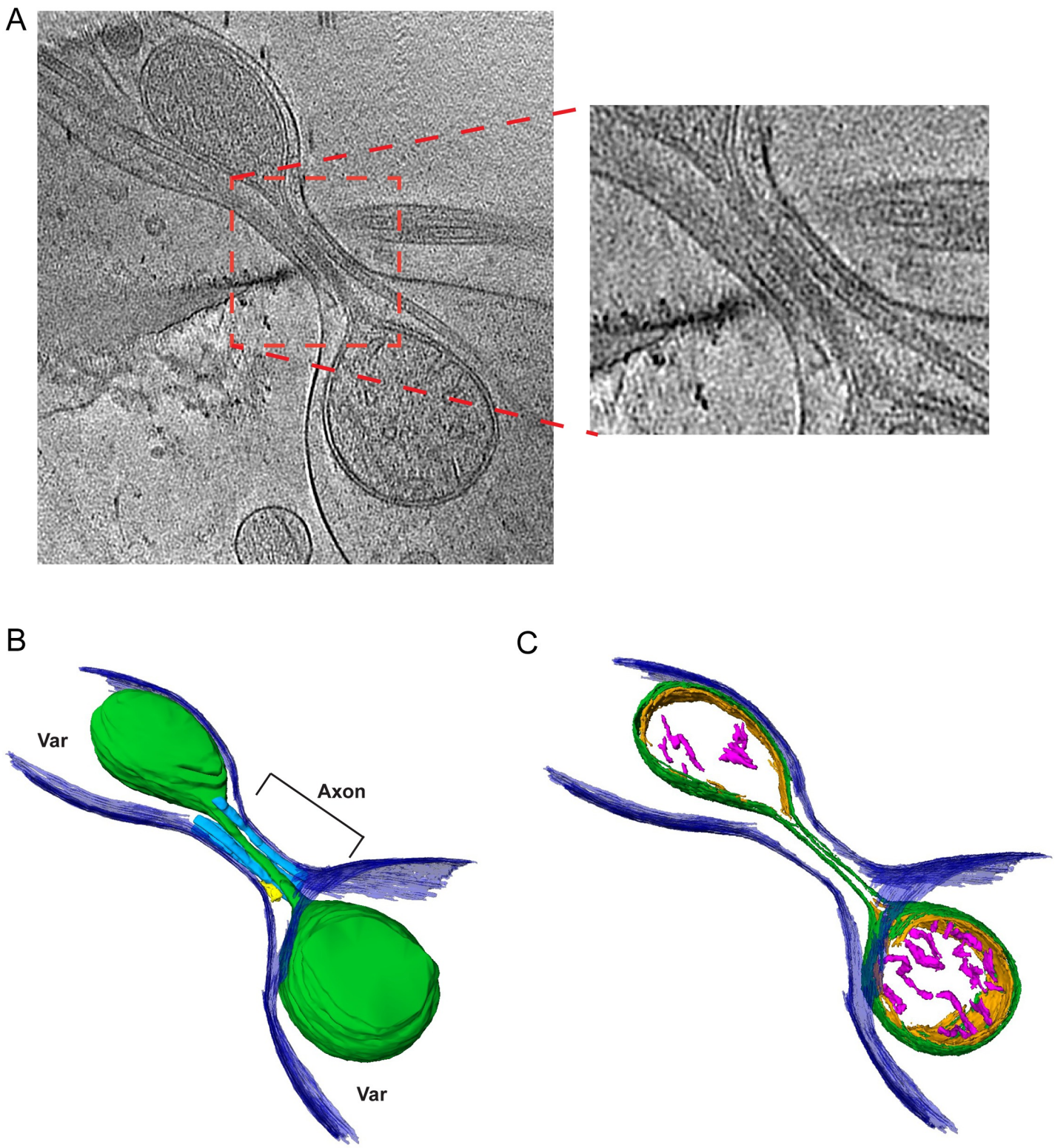

Fig 4. Structural features of a mitochondrion captured spanning 2 varicosities ("Var"). (A) A 10-nm slice through a 3D tomographic reconstruction showing a mitochondrion spanning 2 closely spaced varicosities connected by a short (approximately 100 nm) axon segment. An expanded region of the red box shown in (A) reveals the tubulated nature of the portion of the mitochondrion within the axon segment. Microtubules can be seen running parallel to the tubulated portion of the mitochondrion. (B) shows a surface rendered version highlighting the plasma membrane (purple), microtubules (blue), small segment of ER (yellow), and mitochondria (green). (C) is the same mitochondrion as in (B), displaying distinct segmentation of the outer membrane (green), inner membrane (orange), and cristae (pink).

https://doi.org/10.1371/journal.pbio.2006169.g004

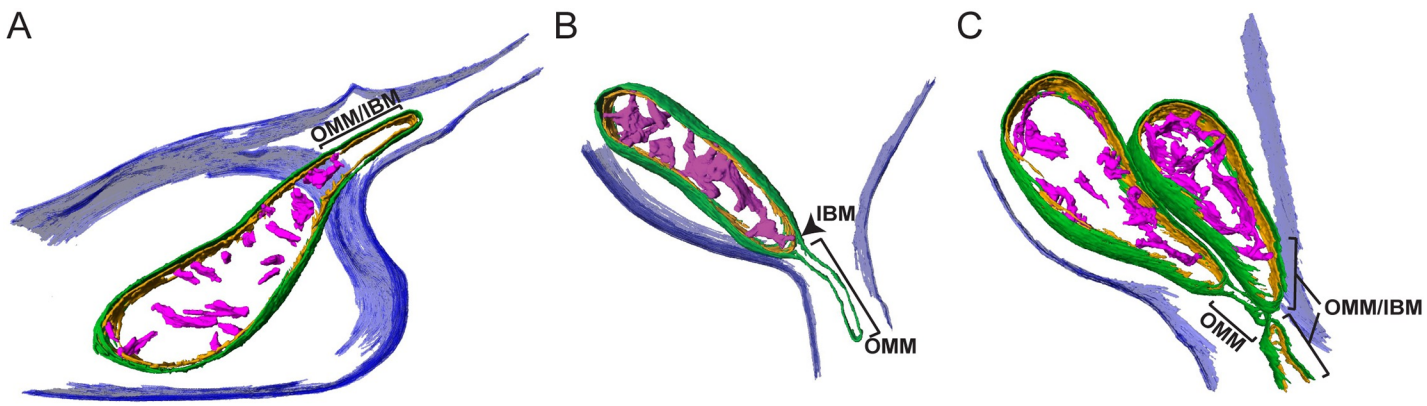

Fig 5. Mitochondrial membranes display distinct morphological features at the boundaries of varicosities and axons with limited physical dimensions. (A–C) To highlight the membrane organization of the mitochondria shown in Fig 3A–3C, the cristae and inner and outer membranes of the 3D reconstructions were segmented. (A) IMMs and OMMs remain in close apposition within the narrowed portion of this mitochondrion resident in the axon. (B) OMM is separated from the inner membrane, creating a distinct "matrix-free" compartment in this portion of the mitochondria residing in the axon. (C) Three mitochondria near the varicosity/axon junction show distinct internal membrane organization. The left mitochondrion shows a portion of outer membrane separated from the inner membrane, while the top right mitochondrion is narrowed near the axon junction, but the inner and outer membranes remain in apposition. A short tip of a third mitochondrion is partially captured at the edge of the tomogram that also shows inner and outer membranes together. Plasma membrane (dark blue), OMM (dark green), mitochondrial IBM (orange), cristae (pink). IBM, inner boundary membrane; IMM, inner mitochondrial membrane; OMM, outer mitochondrial membrane.

https://doi.org/10.1371/journal.pbio.2006169.g005

(green) membranes can be seen narrowing as they enter the restricted axonal space. Cristae (pink) are largely absent from this narrowed portion of the mitochondrion (approximately 69 nm in diameter) residing in the axon. Second, the outer membrane was observed to separate from the inner membrane, leaving a space free of the inner membrane and matrix of the mitochondrion (Fig 5B). Thus, it appears the IMM does not always remain in apposition with the OMM within the rather dramatic tubulation evident of the outer membrane residing within the restricted space of the axon. Two out of the 8 representations of mitochondria displaying these atypical morphological features in our data set also show the OMM separated from the IMM. S11 Movie shows the segmented model of the 3 mitochondria in Figs 3C and 5C. The left mitochondrion can be seen to display the OMM separated from the IMM, while the right mitochondrion displays the OMM and IMM in juxtaposition, demonstrating the occurrence of both events in 1 varicosity/axon boundary area.

Discussion

Although the transport of mitochondria within axons has been widely studied, the potential morphological adaptation of these large organelles to restricted physical dimensions and available space within axons has not been discussed [18,27,28]. The current study provides insight into spatial environments within presynaptic varicosities and thin axons of cryopreserved hippocampal neurons, unperturbed by fixation or stains via 3D cryo-ET. Distinct morphological characteristics of mitochondria were revealed at the boundaries between large varicosities and axon segments with limited physical dimensions (approximately 80 nm). To our knowledge, this is the first study to describe such atypical mitochondrial morphologies apparently influenced by the limitations of physical space within thin axons. Additionally, the 3D reconstruction and segmentation of mitochondrial ultrastructure revealed distinct morphological features between the IMM and OMM at spatially restricted axonal/varicosity boundaries, suggesting possible differential regulation of each membrane during these morphological adaptations.

Axon morphology can be widely variable depending on brain region. En passant boutons are common in axons of the hippocampus and cortex, giving rise to heterogeneous axon morphologies with presynaptic varicosities distributed along thin, unmyelinated axons [3–7]. As axons and synaptic varicosities are dynamic, heterogeneous environments that can be occupied by organelles and molecules differing in size and number, it is important to consider whether available space within the axon may constrain motility or transport of large cargo, such as mitochondria. Using the advantages of cryo-ET, we were able to capture the static spatial environments in thin axons and presynaptic varicosities of cultured hippocampal neurons to examine organelle characteristics and distribution. Mitochondria, in particular, at an average of 250 nm in diameter, presented a clear spatial challenge to inhabit axons that are, on average, 3 times smaller (approximately 80 nm). In the 3D segmentation of mitochondria residing at the boundary between the larger presynaptic varicosity and thin, adjoining axon segments, we observed mitochondria displaying atypical morphological features. Mitochondria displayed a normal morphology within the varicosity and a narrowed tubulated portion, creating a "tip" that existed in the narrowed space within the axon. In some cases, this narrowed portion of the mitochondrion was smaller than the inner boundary of the axonal plasma membrane, suggesting that additional material, not apparent in the tomograms, might further constrain the available space within the axon. The ability of mitochondria to display morphological diameters near 20 nm when challenged with limiting available space within axons is surprising and suggests mitochondrial morphology may be more adaptable in nature than previously considered. Although it is important to emphasize that our methodology does not address temporal dynamics of mitochondria within axons, these observations highlight the potential for the adaptability of mitochondrial morphology and present interesting questions to the mechanisms that may be involved.

Movement of intracellular cargo and transport within axons is mediated by microtubule-associated motor proteins that create the driving force necessary to pull organelles through the cytoplasm in axons and varicosities [11,28]. Specifically, kinesin and dynein motor proteins exert a mechanical force on the mitochondrion to drive polarity-directed movement within axons through interactions with OMM and adaptor proteins, such as Mitochondrial Rho GTPase (Miro) and Milton [29]. We speculate that directional forces induced by motor proteins may drive the morphological features of the mitochondrial membrane, as observed in the current study. Kinesins, in particular, are known to induce membrane deformation or tubulation in in vitro reconstituted membranes [30,31]. A recent study also described similar thin tubulation of mitochondria that is mediated by Kinesin-I Heavy Chain (encoded by KIF5B gene) [32]. The influence of mechanical forces on mitochondrial membrane dynamics was recently demonstrated by the recruitment of mitochondrial fission machinery and subsequent division at sites of induced physical constriction [33]. In fact, it is also possible that recruitment of such machinery would lead to the production of fission intermediates of the mitochondria of reduced size that would facilitate their movement through axons. If so, appropriate machinery would have to be present in adjacent varicosities for the reassembly of mitochondria. Although the distinct morphological features of mitochondria in axons observed in our static, cryopreserved tomographic reconstructions cannot address dynamics for transport, whether force-driven microtubule interactions play a role is an interesting possibility. Additionally, it is also possible that neuronal activity might influence the structure of varicosities, axons, or mitochondria that would impact the magnitude of this problem. In this context, a recent report analyzing varicosities and axons in hippocampal slices showed that high-frequency stimulation of axons increased the size of varicosities and axons [34], although the peak effects on size were relatively modest (an approximately 5% increase in varicosity/axonal diameter). Thus,

further investigation into the precise mechanisms involved in the regulation of space within axons and mitochondrial morphological adaptations within the available space is warranted.

Mitochondrial function is highly dependent on the unique architecture of the IMM, in which the respiratory complexes along with ATP synthase are concentrated in formations of distinct compartments, termed cristae [26,35–37]. Classic and more recent studies examining inner membrane morphology and cristae formation have shown distinct ultrastructural features in states of high cellular energy demands; however, whether inner membrane structure changes occur correspondingly with gross morphological changes (excluding those involved in mitochondrial fission or fusion) is not well defined [24–26,38–41]. Therefore, we questioned whether the significant reduction in size of mitochondria within the physically restrictive axonal space also affected their internal structure. Segmentation of cristae and the IBM, distinct components of the IMM, revealed intriguing differences in the relationship between internal structure and the OMM. In some cases, the IBM remained in close apposition with the OMM at the narrowed tip of the mitochondrion in the axon. Interestingly, this area was also void of cristae, whereas cristae structure remained unperturbed in the portion of the mitochondrion that resided in the varicosity, suggesting possible differential regulation of cristae compartments with adaptation to the limited space within axons. Conversely, a few mitochondria displayed a dissociation of the IMM and OMM, in which the outer membrane was no longer in apposition with the IBM but distinctly separated in the narrowed tip of the mitochondrion, creating a "matrix-free" space. The IBM and cristae remained intact and unperturbed within the portion of the mitochondrion residing in the varicosity. The visualization of the 3D ultrastructure of mitochondria displaying these morphological features within spatially restricted axons suggests a potentially new instance of structural remodeling of the IMM. Mechanistically, this observation generates several interesting questions to the regulation and dynamic nature of mitochondrial ultrastructure, as well as the functional status of mitochondria in different axonal compartments. Although mechanisms for regulating inner membrane morphology remain incompletely defined, recent research has provided insight into some mechanisms involved in the regulation of cristae structure and IMM morphology [25,37, 42,43]. In addition to optic atrophy 1 (Opa1), the primary IMM fusion protein, ATP synthase and the mitochondrial contact site and cristae organizing system (MICOS) exhibit membrane-bending functions and are proposed to determine curvature of the cristae membrane [37,38]. MICOS components have also been implicated in regulating cristae morphology, as well as inner–outer membrane tethering, which could be a potential mechanism driving the differences in inner–outer membrane apposition or dissociation observed in the present study [44,45]. Moreover, distinct events of IMM constriction independent from the OMM have also recently been observed that are driven by increased mitochondrial matrix calcium levels [46–48]. Thus, there is some evidence at the cellular level for differential morphological regulation of the inner and outer membranes. The 3D reconstructions of the OMM, IBM, and cristae in the cryopreserved axon and the observed dissociation between membrane morphologies in the current study lend support for the notion that the OMM and IMM can be remodeled independently. Functionally, the observed changes in cristae and IMM morphology also pose the question as to whether the lack of cristae or adaptation of the IMM influence the functional capacity of these mitochondria. Although the technical limitations of measuring mitochondrial function in relation to mitochondrial structure are challenging, these will be critical investigations in uncovering the dynamic and adaptive nature of the IMM and regulation of mitochondrial function in axons.

The importance of mitochondrial dynamics and synaptic localization to support neuronal function is well recognized (for reviews, see [17,18,49]). Mitochondria must traffic through axons and populate distal synapses to mitigate local energy depletion and maintain calcium

homeostasis required for vesicle release and recycling [16,50,51]. Additionally, mitochondria undergo active fission, fusion, and mitophagy and maintain contact with other organelles to communicate, functionally adapt, and maintain quality control within the local environment. Thus, disruptions in mitochondrial motility and dynamic behaviors can be detrimental to synaptic communication, plasticity, and survival and have been implicated in several neurodegenerative processes (reviewed in [17,29,52]). The current study highlights the potential implications for spatial restrictions dictated by axon morphology to influence mitochondrial morphology and potentially motility within the axon. These findings offer new perspectives on the physical and spatial influence of the cellular environment on mitochondrial morphology and highlight the remarkable structural plasticity of mitochondria to adapt to the limited available space within axons. Given the importance of membrane structure for mitochondrial function and the necessary transport of mitochondria for maintaining synaptic health and neurotransmission, these findings have far-reaching implications for mitochondrial and neuronal biology. Future research will be essential to gain mechanistic insight to regulation of structural changes at mitochondrial membranes and the influence of morphological adaptations of mitochondria during axonal transport.

Materials and methods

Neuronal culture and cryopreservation

Primary neuronal cultures were prepared from E18 rat hippocampi. All protocols involving vertebrate animals were approved by the Institutional Animal Care and Use Committee prior to initiating the studies. Briefly, pooled hippocampi were digested with papain for 20 min at 37˚C and then triturated with a 10-ml pipet. Cells were counted and diluted in Opti-MEM containing 20 mM glucose to a density of 1.5×10^5/ml. Two hundred mesh gold grids covered with Quantifoil 2/1 carbon were placed in 35-mm glass-bottom Mat-Tek dishes and were treated overnight with 100 μg/ml poly-D-lysine. The dishes were then washed 3× with sterile water before plating cells at a density of 1.5×10^6/dish. After letting the cells attach for 1 hr at 37˚C/5% CO_2, the media were exchanged for Neurobasal A supplemented with 2% B-27 (Life Technologies), GlutaMAX (Thermo Scientific, Waltham, CA, United States), and penicillin-streptomycin (Sigma, St. Louis, MO, US) and incubated for 10 d at 37˚C/5% CO_2.

To cryopreserve intact neurons, the grids were lifted from the Mat-Tek dishes, and 5 μL of Neurobasal media containing BSA-coated 10-nm gold fiducials were applied. Fiducial gold facilitates tracking during image acquisition of tilt series and alignment of image frames during postacquisition processing. After manual blotting, the grids were plunged into liquid ethane cooled with liquid N_2. The entire process between removal of the grid from the culture dish and plunge freezing was on average approximately 30 s but never more than 60 s. Cryopreserved grids were stored in liquid N_2 until use.

Immunocytochemistry

Immunostaining of neurons grown on Quantifoil grids was accomplished by fixing the neurons at 10 d post plating in freshly prepared 4% paraformaldehyde in 0.1 M phosphate buffer, pH 7.4, for 10 min at room temperature. The fixative was removed and reaction quenched with 5 min of incubation in 50 mM glycine in 0.1 M phosphate buffer, pH 7.4. Neurons were permeabilized with 0.5% TX-100 in 0.1 M phosphate buffer, pH 7.4, for 15 min and then nonspecific sites blocked with Blocking buffer (2% normal goat serum, 1% BSA, 0.1% TX-100 in 0.1 M phosphate buffer, pH 7.4) for 30 min. Primary antibodies were diluted 1:1,000 in Blocking buffer and incubated for 1 hr at room temperature. Primary antibodies included a monoclonal antibody to CaMKIIα (created in our lab; [53]) and a rabbit polyclonal antibody to

synapsin 1 (Synaptic Systems). Grids were then washed 3×, 5 min each, with Wash buffer (0.2% normal goat serum, 0.1% BSA, 0.01% TX-100 in 0.1 M phosphate buffer, pH 7.4). Grids were then incubated in 1:500 dilution of Alexa 488 labeled goat anti-mouse IgG and Alexa 568 labeled goat anti-rabbit IgG diluted in Blocking buffer for 30 min at room temperature. Grids were washed 3× for 5 min each in Wash buffer, once in 0.1 M phosphate buffer, pH 7.4, and then mounted in Fluoromount anti-fade mounting compound. Bright-field and fluorescent images were collected with a 10× or 40× magnification using a 0.9 NA water immersion lens on a Zeiss inverted microscope using an Andor Zyla 4.0 CMOS camera. Exposure time, shutter, and filter wheel (Sutter Instrument) were controlled through Metamorph software (Molecular Devices).

Cryo-ET

For tomographic data collection, single-axis tilt series were collected from −50˚ to +50˚ in 3˚ increments at approximately −8 μm under focus on an FEI Polara G2 operated at 300 kV and equipped with a Gatan K2 Summit direct electron detector operated in photon counting mode. Data collection was performed in a semiautomated fashion using Serial EM software operated in low-dose mode [54]. Briefly, areas of interest were identified visually, 8 × 8 montages were collected at low magnification (2,400×), and then individual points were marked for automated data collection. Data were collected at either 8.5 or 4.5 Å/pixel. Movies of 8–10 dose-fractionated frames were collected at each tilt angle, and the electron dose spread across all images was limited to a total dose of $<100\ e^-/Å^2$ per tilt series. There is a "missing wedge" of information in the reconstructions due to the inability to collect tilt series through a full 180˚ (+/−90˚) of stage tilting. Additionally, as the stage is tilted, the electron path through the sample increases, decreasing the contrast and quality of the high tilt images. For our system, tilting the stage +/−50˚ was found to be an optimal compromise. The missing wedge leads to anisotropic resolution producing elongation and blurring in the Z-dimension, and tomographic reconstructions need to be interpreted with acknowledgment of this limitation.

Tomographic reconstruction and segmentation

Each tomographic data set was drift corrected with MotionCorr2 [55], and stacks were rebuilt and then aligned using IMOD [56,57]. Tomograms of the aligned stacks were then reconstructed using TOMO3D [58,59]. Contrast was enhanced using SIRT reconstruction implemented in TOMO3D.

Reconstructed tomograms were further processed using the median, nonlocal means and Lanczos filters in Amira (FEI, ThermoFisher Scientific) for manual and semiautomated segmentation. Segmentation was accomplished by manually tracing membranes for each Z slice of the tomographic data set. Membranes were identified and segmented with reference to visualization in all 3 dimensions (X, Y, and Z). The brush tool was primarily used in manual segmentation. When possible, masking approaches were also used in combination with density thresholding for semiautomated segmentation. After segmentation, smoothing tools were employed for the manual tracings, and surfaces were rendered for model construction. All measurements (length and diameter) were performed in either Amira using the 3D measurement tool or in IMOD.

Supporting information

S1 Data. Underlying data for Table 2.
(XLSX)

S1 Fig. Two-dimensional images from tomographic reconstructions of different membrane-bound organelles observed in the varicosities of cryopreserved hippocampal neurons. (A) mitochondrion, (B) MVB and vesicles (arrowheads). (C) ER and an unidentified membrane-bound compartment (arrowhead), (D) Autophagosome, (E) Lamellar body. Scale bar = 200 nm. ER, endoplasmic reticulum; MVB, multivesicular body
(TIF)

S2 Fig. Different populations of mitochondrial cristae ultrastructures in varicosities. (A) Representations of mitochondria displaying thin, tubulated cristae. (B) Representations of mitochondria displaying thick, unstructured cristae. Populations were identified based on full 3D tomographic reconstructions. Scale bar = 200 nm.
(TIF)

S1 Movie. Animation of the 3D tomographic reconstruction and overlay of the segmented structures in Fig 2. Scale bar = 200 nm.
(ZIP)

S2 Movie. Animation demonstrating space within an axon encountered by a mitochondrion presented in the X dimension. The 3D tomographic reconstruction corresponds to Figs 3B and 5B. Scale bar = 200 nm.
(ZIP)

S3 Movie. Animation of the 3D tomographic reconstruction and overlay of the segmented structures in Fig 3A. The 3D tomographic reconstruction also corresponds to Fig 5A. Scale bar = 200 nm.
(ZIP)

S4 Movie. Movie of the tilt series of the tomographic data set corresponding to Figs 3A and 5A. Scale bar = 200 nm.
(ZIP)

S5 Movie. Movie of the 3D tomographic reconstruction corresponding to Figs 3B and 5B. Scale bar = 200 nm.
(ZIP)

S6 Movie. Movie of the tilt series of the tomographic data set corresponding to Figs 3C and 5C. Scale bar = 200 nm.
(ZIP)

S7 Movie. Movie of a mitochondrion at a spatially restricted axonal/varicosity boundary. Scale bar = 200 nm.
(ZIP)

S8 Movie. Movie of an additional mitochondrion at a spatially restricted axonal/varicosity boundary. Scale bar = 200 nm.
(ZIP)

S9 Movie. Movie of the 3D tomographic reconstruction corresponding to Fig 4. Scale bar = 200 nm.
(ZIP)

S10 Movie. Movie of a 3D tomographic reconstruction displaying a mitochondrion spanning a short axon segment and residing in 2 varicosities. Scale bar = 200 nm.
(ZIP)

S11 Movie. Animation of the 3D tomographic reconstruction and overlay of the segmented membranes of mitochondria in Fig 3D. Scale bar = 200 nm.
(ZIP)

Acknowledgments

The authors would like to acknowledge Dr. Andrey Tsvetkov, Ndidi Uzor, and Felix Moruno Manchon for help with primary neuronal cultures. We would also like to thank Dr. Michael Beierlein, Dr. Richard Youle, and Dr. Matt Swulius for advice on the manuscript.

Author Contributions

Conceptualization: Tara D. Fischer, M. Neal Waxham.

Data curation: Tara D. Fischer, M. Neal Waxham.

Formal analysis: Tara D. Fischer.

Investigation: Tara D. Fischer, M. Neal Waxham.

Methodology: Tara D. Fischer, Jun Liu, M. Neal Waxham.

Project administration: Tara D. Fischer.

Resources: Pramod K. Dash, Jun Liu, M. Neal Waxham.

Software: Tara D. Fischer, Jun Liu, M. Neal Waxham.

Supervision: Pramod K. Dash, M. Neal Waxham.

Validation: Tara D. Fischer, M. Neal Waxham.

Visualization: Tara D. Fischer.

Writing – original draft: Tara D. Fischer, M. Neal Waxham.

Writing – review & editing: Tara D. Fischer, Pramod K. Dash, Jun Liu, M. Neal Waxham.

References

1. Debanne D. Information processing in the axon. Nature Reviews Neuroscience. 2004; 5:304–16. https://doi.org/10.1038/nrn1397 PMID: 15034555.
2. Ishizuka N, Weber J, Amaral DG. Organization of intrahippocampal projections originating from CA3 pyramidal cells in the rat. The Journal of Comparative Neurology. 1990; 295:580–623. https://doi.org/10.1002/cne.902950407 PMID: 2358523.
3. Li X-G, Somogyi P, Ylinen A, Buzsáki G. The hippocampal CA3 network: An in vivo intracellular labeling study. Journal of Comparative Neurology. 1994; 339:181–208. https://doi.org/10.1002/cne.903390204 PMID: 8300905.
4. Shepherd GM, Harris KM. Three-dimensional structure and composition of CA3—>CA1 axons in rat hippocampal slices: implications for presynaptic connectivity and compartmentalization. J Neurosci. 1998; 18(20):8300–10. PMID: 9763474.
5. Westrum LE, Blackstad TW. An electron microscopic study of the stratum radiatum of the rat hippocampus (regio superior, CA 1) with particular emphasis on synaptology. J Comp Neurol. 1962; 119:281–309. PMID: 14000149.
6. Muller D, Nikonenko I. Dynamic presynaptic varicosities: A role in activity-dependent synaptogenesis. Trends in Neurosciences. 2003; 26:573–5. https://doi.org/10.1016/j.tins.2003.08.010 PMID: 14585594.
7. Shepherd GMG, Raastad M, Andersen P. General and variable features of varicosity spacing along unmyelinated axons in the hippocampus and cerebellum. Proceedings of the National Academy of Sciences. 2002; 99:6340–5. https://doi.org/10.1073/pnas.052151299 PMID: 11972022.

8. Berbel P, Innocenti GM. The development of the corpus callosum in cats: a light- and electron-microscopic study. J Comp Neurol. 1988; 276(1):132–56. https://doi.org/10.1002/cne.902760109 PMID: 3192762.
9. Anderson JC, Martin KAC. Does bouton morphology optimize axon length? Nature Neuroscience. 2001; 4:1166–7. https://doi.org/10.1038/nn772 PMID: 11713473.
10. Conde C, Cáceres A. Microtubule assembly, organization and dynamics in axons and dendrites. Nature Reviews Neuroscience. 2009; 10:319–32. https://doi.org/10.1038/nrn2631 PMID: 19377501.
11. Saxton WM, Hollenbeck PJ. The axonal transport of mitochondria. Journal of Cell Science. 2012; 125:2095–104. https://doi.org/10.1242/jcs.053850 PMID: 22619228.
12. Fernández-Busnadiego R, Schrod N, Kochovski Z, Asano S, Vanhecke D, Baumeister W, et al. Insights into the molecular organization of the neuron by cryo-electron tomography. Journal of Electron Microscopy. 2011; 60:137–48. https://doi.org/10.1093/jmicro/dfr018 PMID: 21844585.
13. Siksou L, Rostaing P, Lechaire J-P, Boudier T, Ohtsuka T, Fejtova A, et al. Three-Dimensional Architecture of Presynaptic Terminal Cytomatrix. Journal of Neuroscience. 2007; 27:6868–77. https://doi.org/10.1523/JNEUROSCI.1773-07.2007 PMID: 17596435.
14. Palade G. The fine structure of mitochondria. The Anatomical record. 1952; 114:427–51. PMID: 12996882.
15. Frey TG, Mannella CA. The internal structure of mitochondria. Trends Biochem Sci. 2000; 25(7):319–24. PMID: 10871882.
16. Rangaraju V, Calloway N, Ryan TA. Activity-driven local ATP synthesis is required for synaptic function. Cell. 2014; 156:825–35. https://doi.org/10.1016/j.cell.2013.12.042 PMID: 24529383.
17. Devine MJ, Kittler JT. Mitochondria at the neuronal presynapse in health and disease. Nature Reviews Neuroscience. 2018; 19:63–80. https://doi.org/10.1038/nrn.2017.170 PMID: 29348666
18. Sheng ZH. The Interplay of Axonal Energy Homeostasis and Mitochondrial Trafficking and Anchoring. Trends in Cell Biology. 2017; 27:403–16. https://doi.org/10.1016/j.tcb.2017.01.005 PMID: 28228333.
19. Sun T, Qiao H, Pan PY, Chen Y, Sheng ZH. Motile axonal mitochondria contribute to the variability of presynaptic strength. Cell Reports. 2013; 4:413–9. https://doi.org/10.1016/j.celrep.2013.06.040 PMID: 23891000.
20. Li Z, Okamoto KI, Hayashi Y, Sheng M. The importance of dendritic mitochondria in the morphogenesis and plasticity of spines and synapses. Cell. 2004; 119:873–87. https://doi.org/10.1016/j.cell.2004.11.003 PMID: 15607982.
21. Wu Y, Whiteus C, Xu CS, Hayworth KJ, Weinberg RJ, Hess HF, et al. Contacts between the endoplasmic reticulum and other membranes in neurons. Proceedings of the National Academy of Sciences. 2017; 114:E4859–E67. https://doi.org/10.1073/pnas.1701078114 PMID: 28559323.
22. Chen X, Winters C, Azzam R, Li X, Galbraith JA, Leapman RD, et al. Organization of the core structure of the postsynaptic density. Proceedings of the National Academy of Sciences. 2008; 105:4453–8. https://doi.org/10.1073/pnas.0800897105 PMID: 18326622.
23. Grabrucker A, Vaida B, Bockmann J, Boeckers TM. Synaptogenesis of hippocampal neurons in primary cell culture. Cell Tissue Res. 2009; 338(3):333–41. https://doi.org/10.1007/s00441-009-0881-z PMID: 19885679.
24. Hackenbrock CR, Caplan AI. Ion-induced ultrastructural transformations in isolated mitochondria. The energized uptake of calcium. J Cell Biol. 1969; 42(1):221–34. PMID: 5795884; PubMed Central PMCID: PMCPMC2107584.
25. Cogliati S, Enriquez JA, Scorrano L. Mitochondrial Cristae: Where Beauty Meets Functionality. Trends in Biochemical Sciences. 2016; 41:261–73. https://doi.org/10.1016/j.tibs.2016.01.001 PMID: 26857402.
26. Cogliati S, Frezza C, Soriano ME, Varanita T, Quintana-Cabrera R, Corrado M, et al. Mitochondrial cristae shape determines respiratory chain supercomplexes assembly and respiratory efficiency. Cell. 2013; 155:160–71. https://doi.org/10.1016/j.cell.2013.08.032 PMID: 24055366.
27. Morris RL, Hollenbeck PJ. Axonal transport of mitochondria along microtubules and F-actin in living vertebrate neurons. Journal of Cell Biology. 1995; 131:1315–26. https://doi.org/10.1083/jcb.131.5.1315 PMID: 8522592.
28. Schwarz TL. Mitochondrial Trafficking in Neurons. Cold Spring Harbor Perspectives in Biology. 2013:1–15. https://doi.org/10.1101/cshperspect.a011304 PMID: 23732472.
29. Sheng Z-H, Cai Q. Mitochondrial transport in neurons: impact on synaptic homeostasis and neurodegeneration. Nature reviews Neuroscience. 2012; 13:77–93. https://doi.org/10.1038/nrn3156 PMID: 22218207.

30. Vale RD, Hotani H. Formation of membrane networks in vitro by kinesin-driven microtubule movement. Journal of Cell Biology. 1988; 107:2233–41. https://doi.org/10.1083/jcb.107.6.2233 PMID: 3143735.

31. Vale RD, Reese TS, Sheetz MP. Identification of a novel force-generating protein, kinesin, involved in microtubule-based motility. Cell. 1985; 42:39–50. https://doi.org/10.1016/S0092-8674(85)80099-4 PMID: 3926325.

32. Wang C, Du W, Su QP, Zhu M, Feng P, Li Y, et al. Dynamic tubulation of mitochondria drives mitochondrial network formation. Cell Research. 2015; 25:1108–20. https://doi.org/10.1038/cr.2015.89 PMID: 26206315.

33. Helle SCJ, Feng Q, Aebersold MJ, Hirt L, Grüter RR, Vahid A, et al. Mechanical force induces mitochondrial fission. eLife. 2017; 6:e30292. https://doi.org/10.7554/eLife.30292 PMID: 29119945.

34. Chereau R, Saraceno GE, Angibaud J, Cattaert D, Nagerl UV. Superresolution imaging reveals activity-dependent plasticity of axon morphology linked to changes in action potential conduction velocity. Proc Natl Acad Sci U S A. 2017; 114(6):1401–6. https://doi.org/10.1073/pnas.1607541114 PMID: 28115721; PubMed Central PMCID: PMCPMC5307438.

35. Pernas L, Scorrano L. Mito-Morphosis: Mitochondrial Fusion, Fission, and Cristae Remodeling as Key Mediators of Cellular Function. Annual review of physiology. 2015; 78:annurev-physiol-021115-105011. https://doi.org/10.1146/annurev-physiol-021115-105011 PMID: 26667075.

36. Ca Mannella, Pfeiffer DR, Bradshaw PC, Moraru II, Slepchenko B, Loew LM, et al. Topology of the mitochondrial inner membrane: dynamics and bioenergetic implications. IUBMB life. 2001; 52:93–100. https://doi.org/10.1080/15216540152845885 PMID: 11798041.

37. Davies KM, Anselmi C, Wittig I, Faraldo-Gomez JD, Kuhlbrandt W. Structure of the yeast F1Fo-ATP synthase dimer and its role in shaping the mitochondrial cristae. Proceedings of the National Academy of Sciences. 2012; 109:13602–7. https://doi.org/10.1073/pnas.1204593109 PMID: 22864911.

38. Tarasenko D, Barbot M, Jans DC, Kroppen B, Sadowski B, Heim G, et al. The MICOS component Mic60 displays a conserved membrane-bending activity that is necessary for normal cristae morphology. The Journal of Cell Biology. 2017; 216:889–99. https://doi.org/10.1083/jcb.201609046 PMID: 28254827.

39. Mannella CA. Structure and dynamics of the mitochondrial inner membrane cristae. Biochimica et Biophysica Acta (BBA)—Molecular Cell Research. 2006; 1763:542–8. https://doi.org/10.1016/j.bbamcr.2006.04.006 PMID: 16730811.

40. Hackenbrock CR. Ultrastructural bases for metabolically linked mechanical activity in mitochondria. I. Reversible ultrastructural changes with change in metabolic steady state in isolated liver mitochondria. J Cell Biol. 1966; 30(2):269–97. PMID: 5968972; PubMed Central PMCID: PMCPMC2107001.

41. Hackenbrock CR. Ultrastructural bases for metabolically linked mechanical activity in mitochondria. II. Electron transport-linked ultrastructural transformations in mitochondria. J Cell Biol. 1968; 37(2):345–69. PMID: 5656397; PubMed Central PMCID: PMCPMC2107416.

42. Kühlbrandt W. Structure and function of mitochondrial membrane protein complexes. BMC biology. 2015; 13:89. https://doi.org/10.1186/s12915-015-0201-x PMID: 26515107.

43. Friedman JR, Mourier A, Yamada J, Michael McCaffery J, Nunnari J. MICOS coordinates with respiratory complexes and lipids to establish mitochondrial inner membrane architecture. eLife. 2015; 2015:1–61. https://doi.org/10.7554/eLife.07739 PubMed PMID: 25918844.

44. Harner ME, Unger AK, Geerts WJC, Mari M, Izawa T, Stenger M, et al. An evidence based hypothesis on the existence of two pathways of mitochondrial crista formation. eLife. 2016; 5:1–25. https://doi.org/10.7554/eLife.18853 PMID: 27849155.

45. Zerbes RM, Der Klei IJV, Veenhuis M, Pfanner N, Laan MVD, Bohnert M. Mitofilin complexes: Conserved organizers of mitochondrial membrane architecture. Biological Chemistry. 2012; 393:1247–61. https://doi.org/10.1515/hsz-2012-0239 PMID: 23109542.

46. Chakrabarti R, Ji WK, Stan RV, Sanz JDJ, Ryan TA, Higgs HN. INF2-mediated actin polymerization at the ER stimulates mitochondrial calcium uptake, inner membrane constriction, and division. Journal of Cell Biology. 2018:1–18. 10.1083/jcb.201709111 PubMed PMID: 29142021.

47. Cho B, Cho HM, Jo Y, Kim HD, Song M, Moon C, et al. Constriction of the mitochondrial inner compartment is a priming event for mitochondrial division. Nature Communications. 2017; 8:15754. https://doi.org/10.1038/ncomms15754 PMID: 28598422.

48. Lee H, Yoon Y. Transient contraction of mitochondria induces depolarization through the inner membrane dynamin opa1 protein. Journal of Biological Chemistry. 2014; 289:11862–72. https://doi.org/10.1074/jbc.M113.533299 PMID: 24627489.

49. Misgeld T, Schwarz TL. Mitostasis in Neurons: Maintaining Mitochondria in an Extended Cellular Architecture. Neuron. 2017; 96:651–66. https://doi.org/10.1016/j.neuron.2017.09.055 PMID: 29096078.

50. Verstreken P, Ly CV, Venken KJT, Koh T-W, Zhou Y, Bellen HJ. Synaptic Mitochondria Are Critical for Mobilization of Reserve Pool Vesicles at Drosophila Neuromuscular Junctions. Neuron. 2005; 47:365–78. https://doi.org/10.1016/j.neuron.2005.06.018 PMID: 16055061.

51. Pathak D, Berthet A, Nakamura K. Energy Failure: Does It Contribute to Neurodegeneration? 2013. https://doi.org/10.1002/ana.24014 PMID: 24038413

52. Itoh K, Nakamura K, Iijima M, Sesaki H. Mitochondrial dynamics in neurodegeneration. Trends in Cell Biology. 2013; 23:64–71. https://doi.org/10.1016/j.tcb.2012.10.006 PMID: 23159640.

53. Waxham MN, Aronowski J, Kelly PT. Functional analysis of Ca2+/calmodulin-dependent protein kinase II expressed in bacteria. J Biol Chem. 1989; 264(13):7477–82. PMID: 2496129.

54. Mastronarde DN. Automated electron microscope tomography using robust prediction of specimen movements. J Struct Biol. 2005; 152(1):36–51. https://doi.org/10.1016/j.jsb.2005.07.007 PMID: 16182563.

55. Zheng SQ, Palovcak E, Armache JP, Verba KA, Cheng Y, Agard DA. MotionCor2: anisotropic correction of beam-induced motion for improved cryo-electron microscopy. Nat Methods. 2017; 14(4):331–2. https://doi.org/10.1038/nmeth.4193 PMID: 28250466; PubMed Central PMCID: PMCPMC5494038.

56. Kremer JR, Mastronarde DN, McIntosh JR. Computer visualization of three-dimensional image data using IMOD. J Struct Biol. 1996; 116(1):71–6. https://doi.org/10.1006/jsbi.1996.0013 PMID: 8742726.

57. Mastronarde DN, Held SR. Automated tilt series alignment and tomographic reconstruction in IMOD. J Struct Biol. 2017; 197(2):102–13. https://doi.org/10.1016/j.jsb.2016.07.011 PMID: 27444392; PubMed Central PMCID: PMCPMC5247408.

58. Agulleiro JI, Fernandez JJ. Fast tomographic reconstruction on multicore computers. Bioinformatics. 2011; 27(4):582–3. https://doi.org/10.1093/bioinformatics/btq692 PMID: 21172911.

59. Agulleiro JI, Fernandez JJ. Tuning the cache memory usage in tomographic reconstruction on standard computers with Advanced Vector eXtensions (AVX). Data Brief. 2015; 3:16–20. https://doi.org/10.1016/j.dib.2014.12.010 PMID: 26217710; PubMed Central PMCID: PMCPMC4509992.